Materials Chemistry and Physics 224 (2019) 129–136

Contents lists available at ScienceDirect

Materials Chemistry and Physics

journal homepage: www.elsevier.com/locate/matchemphys

# Synthesis and electrochemical performance of carbon-coated $Fe_2GeO_4$ as an anode material for sodium-ion batteries

Yuvaraj Subramanian[a], Myung-Soo Park[a], Ganesh Kumar Veerasubramani[a], Yun-Sung Lee[b], Dong-Won Kim[a,*]

[a] Department of Chemical Engineering, Hanyang University, Seoul, 04763, Republic of Korea
[b] Faculty of Applied Chemical Engineering, Chonnam National University, Gwangju, 61186, Republic of Korea

## HIGHLIGHTS

- High-capacity spinel $Fe_2GeO_4$ is synthesized by hydrothermal reaction and calcination.
- $Fe_2GeO_4$ particle is coated with amorphous carbon to improve its cycling stability.
- The $Fe_2GeO_4$@C exhibits a high discharge capacity with good capacity retention.
- The $Fe_2GeO_4$@C can be used as a promising anode material for sodium-ion battery.

## ARTICLE INFO

*Keywords:*
$Fe_2GeO_4$ anode
Carbon coating
$NaCo_{0.5}Fe_{0.5}O_2$ cathode
Sodium-ion battery
Cycling performance

## ABSTRACT

The development of anode materials with high capacity and good cycling stability is one of the state-of-the-art objectives in the field of rechargeable sodium-ion batteries. In this work, we synthesized high-capacity spinel $Fe_2GeO_4$ using a facile hydrothermal method followed by calcination and investigated its electrochemical performance as an anode material for sodium-ion batteries. The $Fe_2GeO_4$ material delivered a high initial discharge capacity of 448.1 mAh $g^{-1}$, but it showed gradual capacity fading with a capacity retention of 67.4% after 50 cycles. Its high initial capacity originated from the high electrochemical activity of Fe caused by its multiple oxidation reactions. To enhance the cycling stability of the $Fe_2GeO_4$, carbon was coated onto the surface of $Fe_2GeO_4$ particles. The carbon-coated $Fe_2GeO_4$ ($Fe_2GeO_4$@C) exhibited an initial discharge capacity of 423.0 mAh $g^{-1}$ with good capacity retention. The sodium-ion full cell was assembled with an $Fe_2GeO_4$@C anode and a $NaCo_{0.5}Fe_{0.5}O_2$ cathode, and the results showed superior cycling performance, demonstrating that the $Fe_2GeO_4$@C can be used as a promising anode material for sodium-ion batteries.

## 1. Introduction

In the growing research field of energy, researchers have intensively investigated electrode materials for rechargeable lithium-ion batteries, which are widely used in portable electronic devices, electric vehicles and energy storage systems due to their high energy density and excellent cycling stability [1–4]. The usage of lithium-ion batteries has increased significantly, which has caused a decrease of lithium sources as well as an increase of the battery cost. Sodium-ion batteries have been considered as an alternative power source for large-scale energy storage, because they have a lot of merits when compared to lithium, such as low cost and a natural abundance. However, the $Na^+$ ion has a slightly larger ionic radius than $Li^+$ ($Na^+$ ion: 1.02 Å and $Li^+$ ion: 0.76 Å), which hinders fast ion diffusion in the electrode [5,6]. Recently, many researchers have been devoted to developing a suitable anode material for sodium-ion batteries. Graphite is a well-known anode material for lithium-ion batteries, but sodium ions cannot be intercalated into graphite [5,7]. On the other hand, hard carbon has been investigated as an anode material for sodium-ion battery, but it exhibits a low reversible capacity of ~300 mAh $g^{-1}$, which leads to a decrease in the energy density of the battery [8,9]. Apart from carbonaceous materials, the conversion and alloying metal oxides such as $Fe_3O_4$, $Co_3O_4$, $Mn_3O_4$, $NiCo_2O_4$, $MnFe_2O_4$, $SnO_2$ and bimetallic oxides and sulfides have been investigated as anode materials for high energy density sodium-ion batteries [10–17]. These conversion-type anode materials have multiple electron transfer reactions, which provide a high theoretical capacity through a one-step conversion reaction.

* Corresponding author.
*E-mail address:* dongwonkim@hanyang.ac.kr (D.-W. Kim).

https://doi.org/10.1016/j.matchemphys.2018.12.007
Received 17 July 2018; Received in revised form 1 December 2018; Accepted 9 December 2018
Available online 10 December 2018
0254-0584/ 

$MO_x + 2x\ Na^+ + 2x\ e^- \leftrightarrow M + Na_2O$ (M = Co, Fe and Ni)

Recently, Valvo et al. reported that a nanostructured $Fe_2O_3$ anode material delivered a specific capacity of 250 mAh $g^{-1}$ at 130 mA $g^{-1}$ over 60 cycles, but it showed gradual capacity fading on repeated cycling [18]. Generally, the transition metal oxides experience serious volume expansion during the sodiation and de-sodiation processes, which causes a lot of problems such as agglomeration of active material and loss in electrical contact between the current collector and the active materials, leading to capacity fading upon continuous cycling [18,19]. To avoid these problems, some strategies have been widely adopted such as reducing the particle size to the nano-level with a porous structure and the use of composites of active materials within a conducting carbon matrix [20–28].

In our study, we synthesized $Fe_2GeO_4$ and investigated its electrochemical performance as an anode for sodium-ion batteries. It is an active anode material that has the conversion and alloying mechanisms of Fe and Ge. Here, Ge can electrochemically react with Na to form NaGe (369 mAh $g^{-1}$), and it has $10^4$ times higher electronic conductivity than silicon [29,30]. The $Fe_2GeO_4$ material delivered a high discharge capacity, but it showed poor cycling stability. To improve its cycling stability, $Fe_2GeO_4$ was coated with carbon through a hydrothermal method. The carbon coating layer acted as a buffering and conducting matrix that restricted the volume change and enhanced the electronic conductivity of the electrode material. As a result, the carbon-coated $Fe_2GeO_4$ ($Fe_2GeO_4$@C) anode material exhibited good electrochemical performance in terms of the discharge capacity, cycling stability and rate capability. To demonstrate its practical application, we assembled a sodium-ion full cell with an $Fe_2GeO_4$@C anode and a $NaCo_{0.5}Fe_{0.5}O_2$ cathode, and the results showed superior cycling performance.

## 2. Experimental

### 2.1. Synthesis of carbon-coated $Fe_2GeO_4$ and $NaCo_{0.5}Fe_{0.5}O_2$ particles

$Fe_2GeO_4$ particles were synthesized by a facile hydrothermal method. The starting precursors were $FeCl_2$, $GeO_2$ and NaOH powder. First, 6 mmol of $FeCl_2$ was dissolved in 20 mL of distilled water. Then, 2 mmol of $GeO_2$ was dispersed in 20 mL of $H_2O$ and 15 mmol of NaOH was added into the solution. The two solutions were mixed well by stirring for 30 min, and the mixed solution was transferred into a Teflon-lined, stainless-steel autoclave kept at 180 °C. After a hydrothermal reaction for 24 h, the autoclave was cooled to room temperature. The obtained precipitate was washed several times with water and ethanol, and then dried at 80 °C for 12 h. The dried sample was then calcinated at 500 °C for 3 h to obtain $Fe_2GeO_4$ particles. Carbon coating of pristine $Fe_2GeO_4$ particles was performed using the hydrothermal method. Initially, 0.4 g of $Fe_2GeO_4$ particles was dispersed in 60 mL of distilled water by ultrasonication, and 0.8 g of glucosamine was added to the dispersion. The solution was transferred to Teflon-lined, stainless steel autoclave held at 140 °C and maintained at that temperature for 12 h. The collected powder was washed several times using distilled water and ethanol. The sample was dried at 80 °C for 12 h and carbonization was carried out at 500 °C for 2 h under an Ar atmosphere to obtain $Fe_2GeO_4$@C particles. As a cathode material, $NaCo_{0.5}Fe_{0.5}O_2$ was prepared by a conventional solid-state reaction. Stoichiometric amounts of $Na_2CO_3$ (1.081 g), $Fe_2O_3$ (0.798 g), and $Co_3O_4$ (0.801 g) were ground together, followed by calcination at 900 °C for 12 h to obtain $NaCo_{0.5}Fe_{0.5}O_2$ particles.

### 2.2. Electrode preparation and cell assembly

The electrode slurry was prepared by mixing active material ($Fe_2GeO_4$ or $Fe_2GeO_4$@C), Ketjen black and carboxymethyl cellulose in the weight ratio of 70:20:10 in water. The slurry was coated onto a Cu foil, and the electrode was dried in a vacuum oven at 80 °C for 12 h. The active mass loading in the electrode was about 2.0 mg $cm^{-2}$. A CR2032-type coin cell was assembled by sandwiching a glass fiber separator (Whatman) between sodium foil (Alfa Aesar 99%) and $Fe_2GeO_4$ (or $Fe_2GeO_4$@C) electrode. The cell was then injected with an electrolyte consisting of 1 M $NaClO_4$ in ethylene carbonate (EC)/propylene carbonate (PC) (1:1 by volume) containing 10 wt.% fluoroethylene carbonate (FEC) (battery grade, PANAX ETEC Co. Ltd.). Karl Fisher titration using a Mettler-Toledo coulometer confirmed that the water content in the electrolyte was less than 20 ppm. A sodium-ion full cell was assembled with an $Fe_2GeO_4$@C anode and a $NaCo_{0.5}Fe_{0.5}O_2$ cathode. The cathode was prepared by casting an N-methyl-2-pyrrolidone (NMP)-based slurry consisting of $NaCo_{0.5}Fe_{0.5}O_2$ (80 wt.%), Ketjen black (10 wt.%), and poly (vinylidene difluoride) (PVdF) (10 wt. %) onto Al foil and drying in a vacuum oven at 110 °C for 12 h. All the cells were assembled in a glove box under an argon atmosphere.

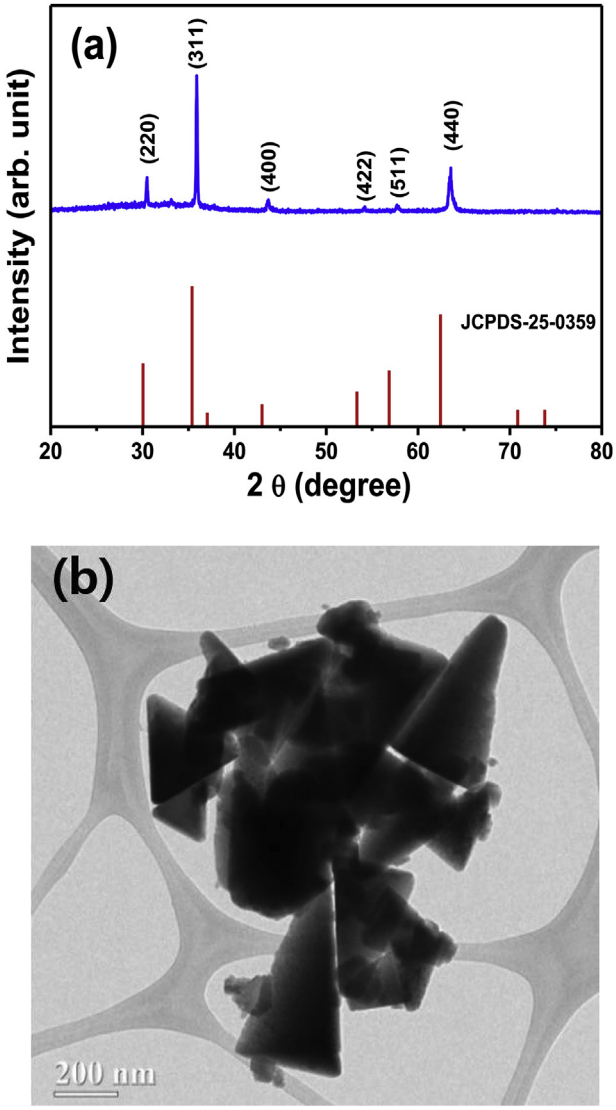


**Fig. 1.** (a) XRD pattern and (b) TEM image of synthesized $Fe_2GeO_4$ particles.

### 2.3. Characterization and measurements

X-ray diffraction (XRD) patterns of the synthesized samples were recorded on a Rigaku Mini Flex X-ray diffractometer using Cu $K_\alpha$ radiation. The morphologies of the samples were examined using a field emission scanning electron microscope (FE-SEM, JEOL JSM-6300) and

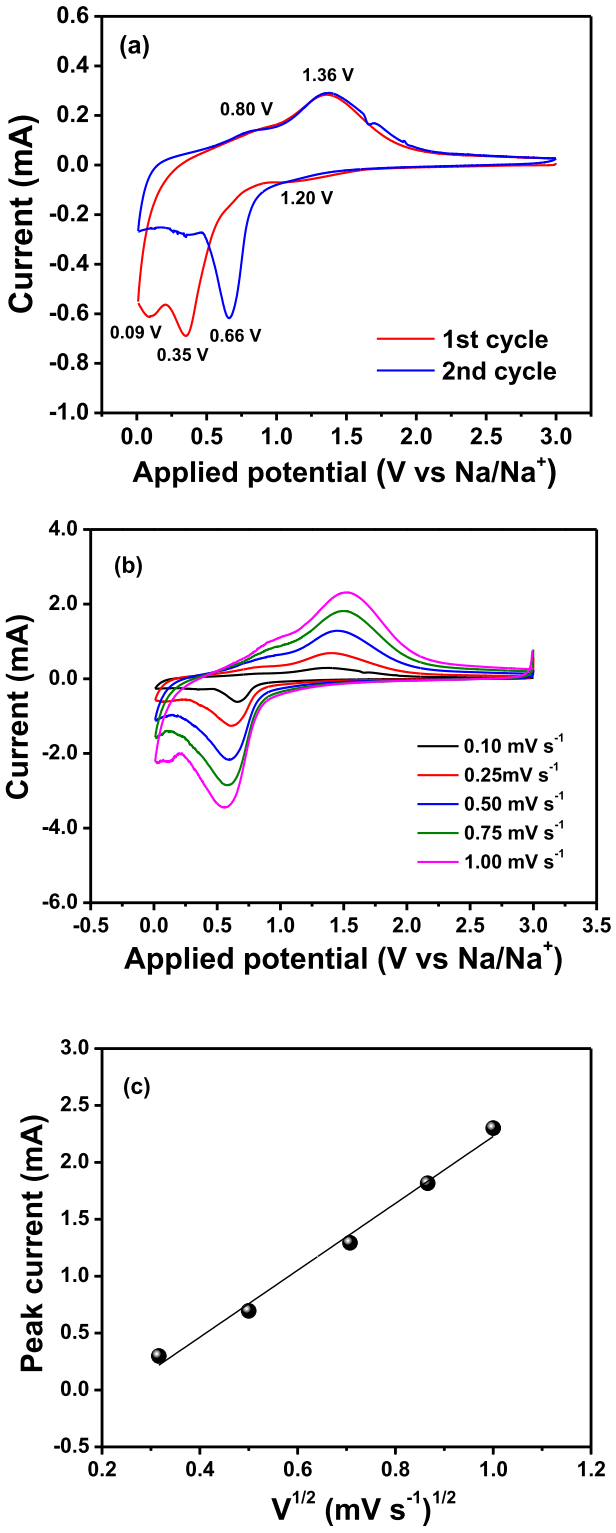


**Fig. 2.** Cyclic voltammograms of the $Fe_2GeO_4$ electrode at (a) 0.1 mV $s^{-1}$ and (b) different scan rates. (c) Peak current versus square root of scan rate.

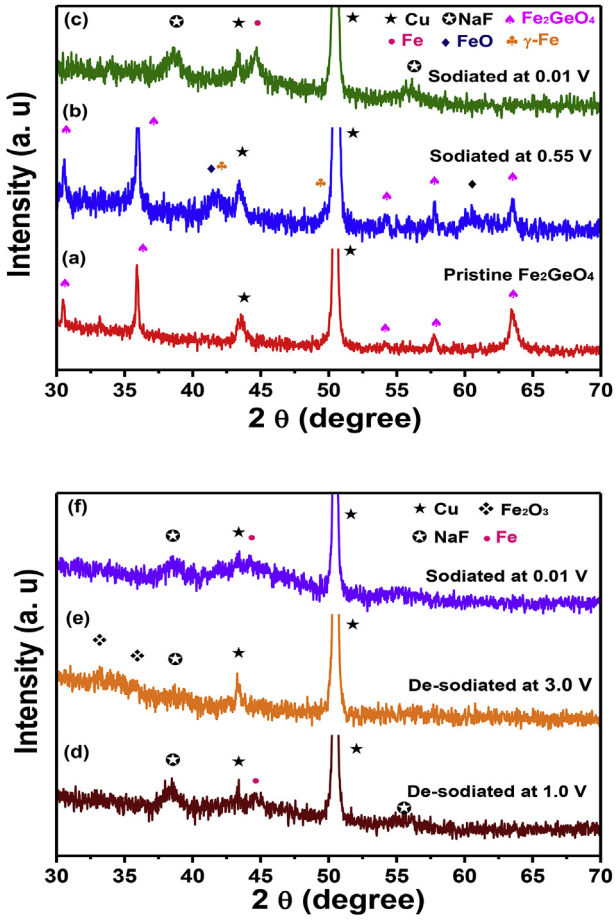


**Fig. 3.** Ex-situ XRD patterns of the $Fe_2GeO_4$ electrode at different states of charge: (a) pristine $Fe_2GeO_4$ electrode, (b) $Fe_2GeO_4$ electrode sodiated at 0.55 V, (c) $Fe_2GeO_4$ electrode sodiated at 0.01 V, (d) $Fe_2GeO_4$ electrode de-sodiated at 1.0 V, (e) $Fe_2GeO_4$ electrode de-sodiated at 3.0 V, and (f) $Fe_2GeO_4$ electrode sodiated at 0.01 V.

a transmission electron microscope (TEM, JEOL, JEM 2100F). X-ray photoelectron spectroscopy (XPS) was performed with a spectrometer having Mg/Al Kα radiation (XPS, VG Multilab ESCA System, 220i). Thermogravimetric analysis (TGA) was carried out using a thermal analyzer (SDT Q600, TA Instrument) in the temperature range from 30 to 800 °C at a heating rate of 5 °C $min^{-1}$. Raman spectrum of the $Fe_2GeO_4$@C particles was obtained using an NRS-3100 laser Raman spectrometer using 532 nm excitation. Cyclic voltammetry (CV) was performed in the potential range of 0.01–3.0 V with counter and reference electrodes of sodium metal at various scan rates (0.1–1.0 mV $s^{-1}$) using a CHI660D electrochemical workstation. A galvanostatic charge and discharge cycling test was conducted at a constant current density in the voltage range of 0.01–3.0 V using battery testing equipment (WBCS 3000, Wonatech) at room temperature.

## 3. Results and discussion

A facile hydrothermal method was used to synthesize $Fe_2GeO_4$ particles using $FeCl_2$ and $GeO_2$ as starting precursors. Fig. 1a presents the XRD pattern of the synthesized $Fe_2GeO_4$ particles. It shows the crystalline peaks at 30.5, 35.9, 43.6, 54.2, 57.7 and 63.6°, which correspond to (220), (311), (400), (422), (511) and (440) lattice planes, respectively. All the diffraction peaks are consistent with the cubic spinel crystal structure of $Fe_2GeO_4$ compound (JCPDS File No. 25–0359). A TEM image of $Fe_2GeO_4$ particles in Fig. 1b shows triangular cube-shaped particles with an average particle size of 500 nm.

The electrochemical charge storage mechanism of $Fe_2GeO_4$ was investigated by CV analysis. Fig. 2a presents the CV curves of the $Fe_2GeO_4$ electrode, which were obtained at the first and second cycle, respectively, in the potential range of 0.01–3.0 V at 0.1 mV $s^{-1}$. The CV curve in the first cathodic cycle shows a small and broad reduction peak around 1.2 V, which corresponds to the reductive decomposition of FEC. After that, two reduction peaks are observed at 0.35 and 0.09 V,

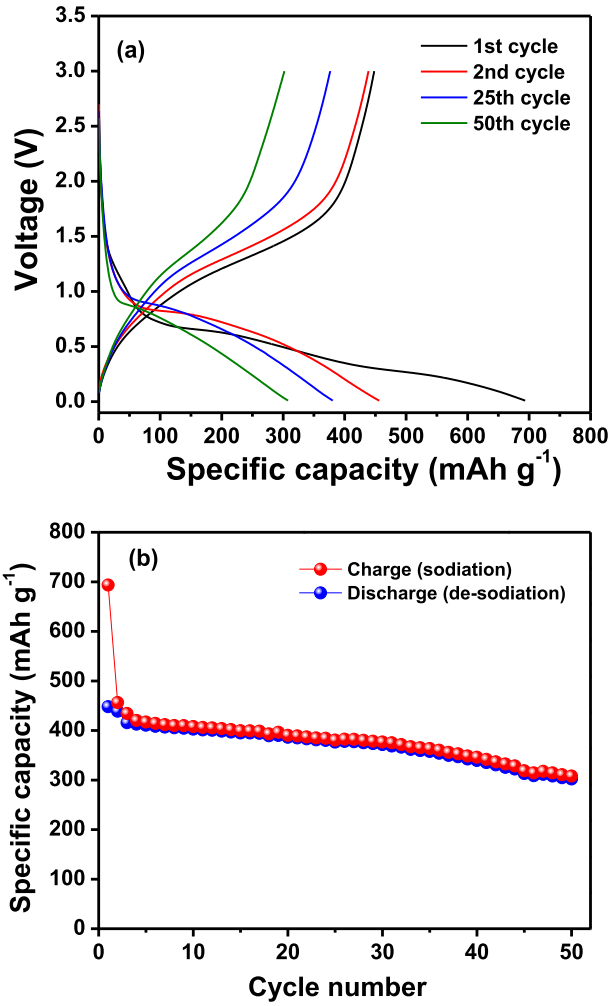


**Fig. 4.** (a) Charge and discharge curves of the $Fe_2GeO_4$ electrode and (b) specific capacities of the $Fe_2GeO_4$ electrode as a function of cycle number (current rate: 100 mA $g^{-1}$, temperature: 25 °C).

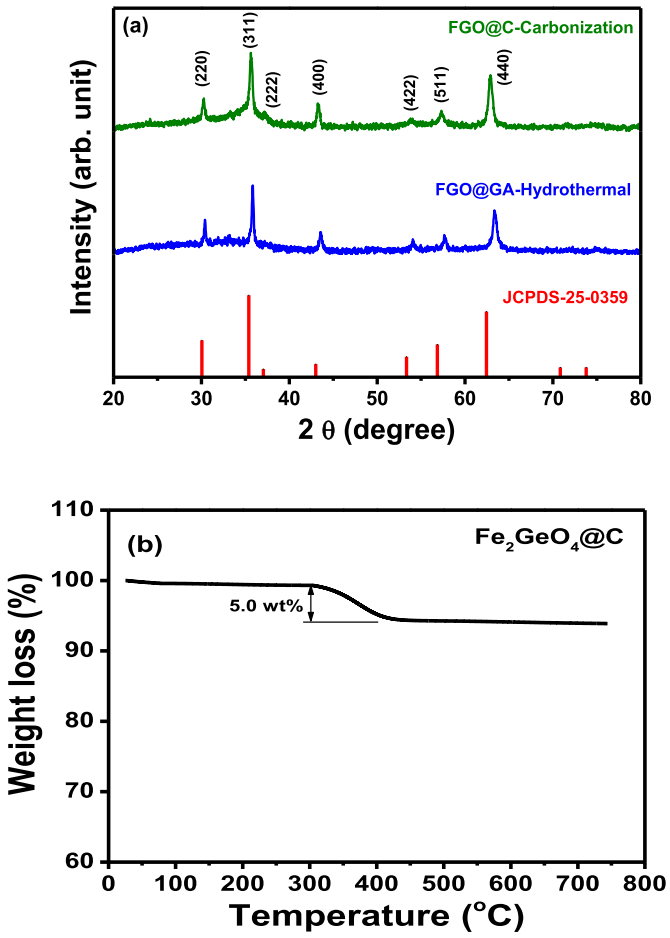


**Fig. 5.** (a) XRD patterns of $Fe_2GeO_4$ particles after the hydrothermal and carbonization processes and (b) TGA curve of $Fe_2GeO_4$@C particles.

which can be ascribed to the reduction of $Fe_2GeO_4$ into its individual constituents ($Fe_2GeO_4 + 8Na^+ + 8e^- \rightarrow 2Fe + Ge + 4Na_2O$) followed by the formation of NaGe ($Ge + Na^+ + e^- \leftrightarrow NaGe$). In the first anodic scan, it shows two oxidation peaks at 0.80 and 1.36 V, which are associated with a two-step oxidation process of $Fe^0$ to $Fe^{2+}$ and $Fe^{3+}$, respectively. In the second cycle, the cathodic peak was observed at 0.66 V, which corresponds to the reduction of $Fe^{3+}$ to $Fe^0$. After the first cycle, stable and reversible redox peaks are observed at 1.36 and 0.66 V, which are attributed to the conversion reaction of $Fe_2O_3$ ($2Fe + 3Na_2O \leftrightarrow Fe_2O_3 + 6Na^+ + 6e^-$). CV curves were obtained at scan rates from 0.1 to 1.0 mV $s^{-1}$, as shown in Fig. 2b. As expected, the current increased with increasing scan rate. The anodic and cathodic peaks were shifted to higher and lower potential, respectively, due to polarization when the scan rate was increased [31]. Fig. 2c illustrates the linear relationship between the peak current and the square root of the scan rate, indicating that the charge storage mechanism is a diffusion-controlled process. The diffusion coefficient was estimated from the slope, using the Randles-Servick equation, to be $3.3 \times 10^{-8}$ $cm^2$ $s^{-1}$ [32,33].

The electrochemical reaction mechanism of $Fe_2GeO_4$ was investigated through ex-situ XRD analysis at different states of charge, as shown in Fig. 3. The peaks observed at 44.5° and 52.0° in the pristine $Fe_2GeO_4$ electrode (Fig. 3a) correspond to Cu current collector. During the 1st sodiation process at 0.55 V (Fig. 3b), new peaks appeared at 41.5° and 41.8°, which can be ascribed to the crystalline peak of FeO and α-Fe, respectively, indicating the reduction of $Fe_2GeO_4$ into its individual element. The peaks of $Fe_2GeO_4$ disappeared at 0.01 V (Fig. 3c), and two new peaks could be observed at 38.7° and 55.8°, which corresponded to NaF produced by decomposition of FEC. These results reveal that electrolyte decomposition and irreversible reaction of $Fe_2GeO_4$ take place during the initial sodiation process. We could not identify the alloying reaction of Ge that may occur in amorphous nature [34]. In the electrode de-sodiated at 1.0 and 3.0 V, Fe was reduced and $Fe_2O_3$ was formed according to the reaction, $2Fe + 3Na_2O \leftrightarrow Fe_2O_3 + 6Na^+ + 6e^-$, as shown in Fig. 3d and e. When the electrode was fully sodiated at 0.01 V (Fig. 3f), the Fe element again appeared due to the reversible reaction of $Fe_2O_3$, indicating the Fe element follows the conversion reaction mechanism after initial formation cycle. These ex-situ XRD results are well consistent with those obtained in cyclic voltammetry.

Galvanostatic charge and discharge cycling of the $Fe_2GeO_4$ electrode was performed at a constant current density of 100 mA $g^{-1}$, and the resulting voltage profiles are shown in Fig. 4a. The $Fe_2GeO_4$ electrode initially delivered a discharge (de-sodiation) capacity of 448.1 mAh $g^{-1}$ with a low coulombic efficiency of 64.6%. The low coulombic efficiency was ascribed to the formation of a solid electrolyte interphase (SEI) layer by reductive decomposition of FEC on the electrode surface and the irreversible reaction of the $Fe_2GeO_4$ electrode. After the first cycle, the coulombic efficiency was increased to 96.2% due to the subsequent reversible reaction of $Fe_2GeO_4$.

Fig. 4b shows the discharge capacities of the $Fe_2GeO_4$ electrode as a function of the cycle number at a current density of 100 mA $g^{-1}$. The $Fe_2GeO_4$ electrode exhibited a discharge capacity of 302.1 mAh $g^{-1}$ with a capacity retention of 67.4% after 50 cycles. The large capacity

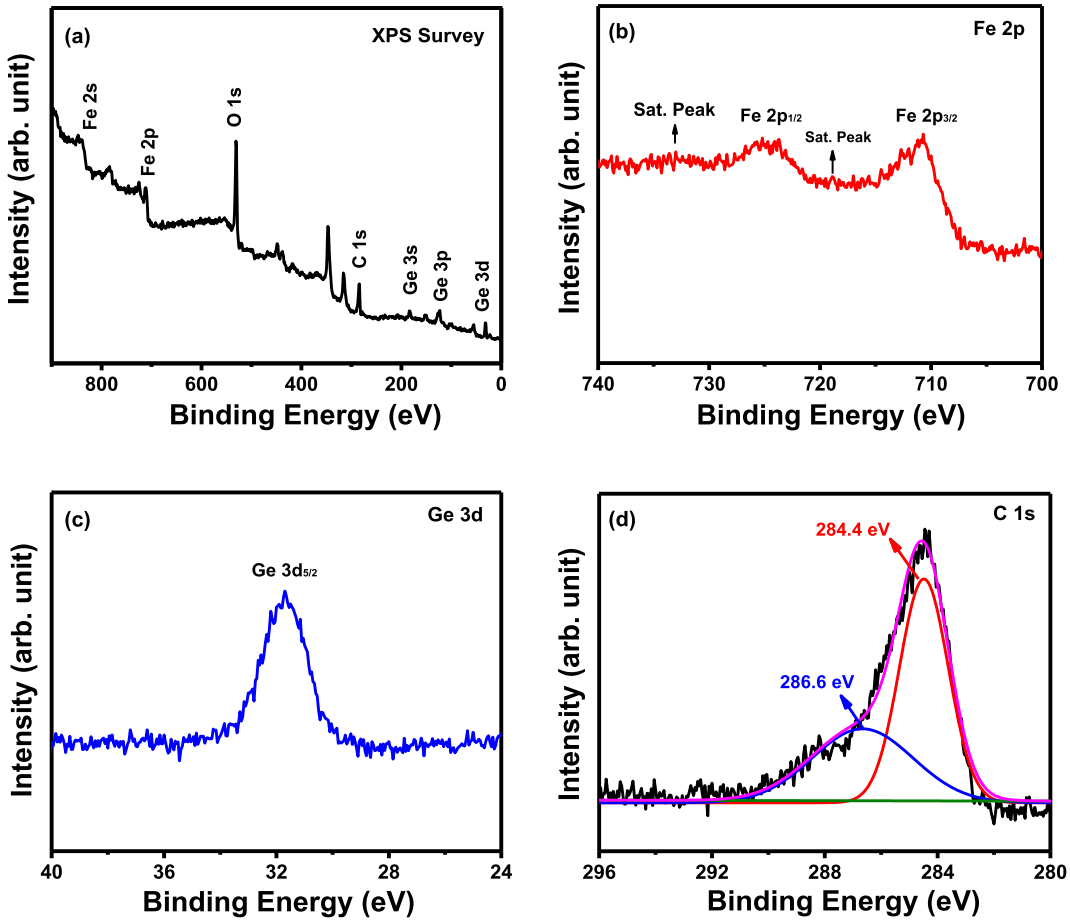


**Fig. 6.** (a) XPS survey, (b) Fe 2p, (c) Ge 3d and (d) C 1s spectra of $Fe_2GeO_4$@C.

fading in the $Fe_2GeO_4$ electrode was related to the mechanical stress caused by the large volume change during the sodiation and de-sodiation processes, leading to a loss of integrity of the electrode [35].

To enhance the cycling stability of the $Fe_2GeO_4$ electrode, carbon was coated on the surface of the $Fe_2GeO_4$ particles, as schematically illustrated in Fig. S1. The XRD pattern of the $Fe_2GeO_4$ particles was obtained after the hydrothermal and carbonization processes. As shown in Fig. 5a, there were no structural changes in the $Fe_2GeO_4$ particles after carbon coating. All the diffraction peaks were well matched with the standard XRD pattern of the cubic crystal structure of $Fe_2GeO_4$ (JCPDS File No-25-0359). The content of carbon on the surface of the $Fe_2GeO_4$ particles was estimated to be 5.0 wt.% by TGA analysis in Fig. 5b. The presence of carbon was further confirmed by Raman spectroscopy. Raman spectrum of $Fe_2GeO_4$@C in Fig. S2 showed two characteristic peaks at 1318 and 1589 $cm^{-1}$, corresponding to the D-band and the G-band, respectively [36–38]. The D-band originated from the scattering from a defect which breaks the basic symmetry of carbon, and the G-band arose from the $sp^2$-hybridized carbon structures. As shown in the figure, the coating layer on $Fe_2GeO_4$ had a higher content of disordered carbon. It has been known that sodium ion diffusion is high in amorphous carbon as compared to graphitic carbon [39,40]. Thus, the amorphous carbon coated on the active $Fe_2GeO_4$ material is expected to enhance sodium ion diffusion as well as accommodate the volume strain. Fig. S3 presents the TEM and high-resolution TEM images of an $Fe_2GeO_4$@C particle. Its enlarged view shows the d-spacing value of 0.16 nm, which is ascribed to the (511) plane of the $Fe_2GeO_4$ cubic crystal. A carbon layer with a thickness of 3–5 nm can be also seen on the surface of the $Fe_2GeO_4$@C particle.

The valence state and functional group of $Fe_2GeO_4$@C was investigated by XPS analysis, and the results are shown in Fig. 6. The XPS survey spectrum of $Fe_2GeO_4$@C in Fig. 6a shows the existence of Fe, Ge, O and C. The deconvoluted Fe 2p spectrum in Fig. 6b presents two characteristic peaks that correspond to the core level spectral lines of Fe $2p_{3/2}$ and Fe $2p_{1/2}$. This reveals the existence of the $Fe^{2+}$ state and a small satellite peak at 733.1 eV, which can be assigned to the $Fe^{3+}$ state in the $Fe_2GeO_4$ compound [41]. The Ge 3d spectrum in Fig. 6c shows a peak at ~31.7 eV indicates the presence of the $Ge^{4+}$ state in the sample [42]. The deconvoluted spectra of carbon 1s in Fig. 6d shows two peaks at 284.4 and 286.6 eV, which are attributed to the C—C bond in aromatic rings and the C—O group, respectively. The C—O bond is formed at the interface between the carbon shell and $Fe_2GeO_4$ core interface, which can facilitate electron transfer between the shell and the core [43].

Cycling performance of the $Fe_2GeO_4$@C electrode was evaluated at a current density of 100 mA $g^{-1}$, and the results are shown in Fig. 7a. In this figure, the specific capacity was obtained after two pre-conditioning cycles. As shown in figure, the $Fe_2GeO_4$@C electrode exhibited an initial discharge capacity of 423.0 mAh $g^{-1}$ and stable cycling behavior. After 100 cycles, the $Fe_2GeO_4$@C electrode delivered a discharge capacity of 376.5 mAh $g^{-1}$, corresponding to a capacity retention of 89.0%, which illustrated that the $Fe_2GeO_4$@C had better capacity retention compared to the pristine $Fe_2GeO_4$ material. The enhanced cycling stability of the $Fe_2GeO_4$@C electrode was because the carbon layer on $Fe_2GeO_4$ particles offered strength to accommodate volume strain during the sodiation and de-sodiation process. The rate capabilities of pristine $Fe_2GeO_4$ and $Fe_2GeO_4$@C were compared at current densities of 100 to 2000 mA $g^{-1}$, as shown in Fig. 7b. The effect of the carbon coating on the rate performance of the electrode was noticeable as the current density was increased. The carbon layer could provide a continuous electronic pathway between the $Fe_2GeO_4$

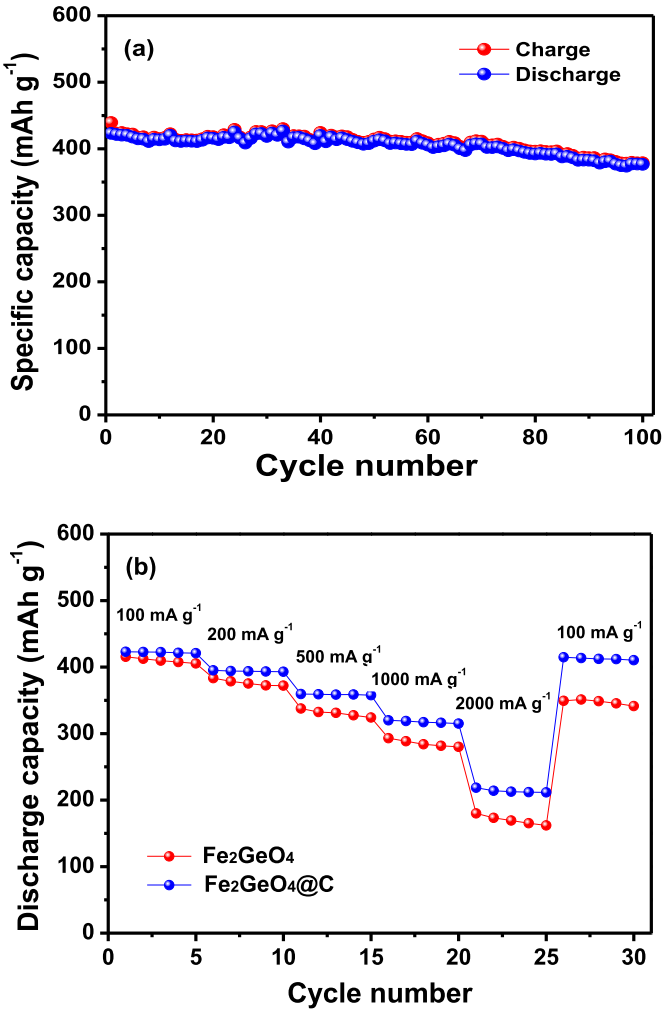


**Fig. 7.** (a) Charge and discharge capacities of the $Fe_2GeO_4$@C electrode as a function of the cycle number (current rate: 100 mA $g^{-1}$, temperature: 25 °C), (b) Discharge capacities of the $Fe_2GeO_4$ and $Fe_2GeO_4$@C electrodes with the current density increasing from 100 to 2000 mA $g^{-1}$ every five cycles.

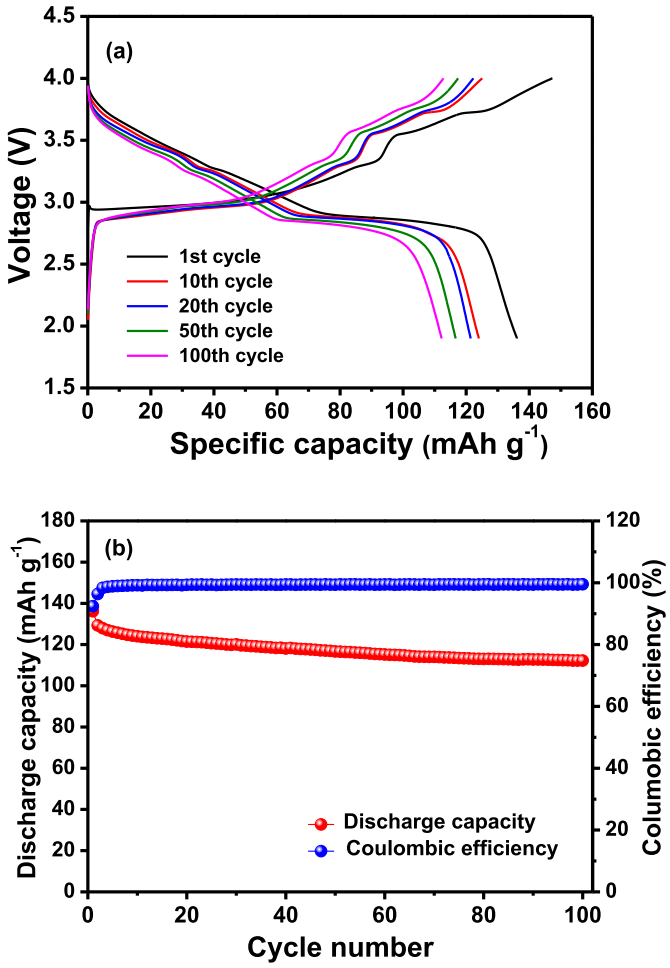


**Fig. 8.** (a) Charge and discharge curves of the $NaCo_{0.5}Fe_{0.5}O_2$ electrode and (b) discharge capacity and coulombic efficiency of the $NaCo_{0.5}Fe_{0.5}O_2$ electrode as a function of the cycle number (current rate: 20 mA $g^{-1}$, cut-off voltage: 1.9–4.0 V).

particles, resulting in an improvement of the rate capability. The $Fe_2GeO_4$@C electrode also retained a high reversible capacity when returned to lower current density (100 mA $g^{-1}$), which assured good cycling stability of the $Fe_2GeO_4$@C electrode material.

The morphology change of $Fe_2GeO_4$@C electrode before and after cycling was investigated by SEM analysis. As depicted in Figs. S4a and S4b, the pristine electrode before cycling exhibited porous structure comprising of conducting carbon and trigonal prism-shaped $Fe_2GeO_4$@C particles. After 100 cycles, some cracks could be observed on the electrode surface due to volume expansion of $Fe_2GeO_4$@C particles during the repeated cycling (Fig. S4c). The initial morphology of $Fe_2GeO_4$@C particles was not retained after cycling, which can be attributed to the conversion and alloying reaction of Fe and Ge element. The electrode surface seemed to smooth after cycling (Fig. S4d), indicating the thin SEI layer was formed on the electrode surface due to the electrolyte decomposition.

For practical applications, the sodium-ion full cell was assembled with an $Fe_2GeO_4$@C anode and a $NaCo_{0.5}Fe_{0.5}O_2$ cathode. The $NaCo_{0.5}Fe_{0.5}O_2$ cathode was prepared via a solid-state reaction, and its XRD pattern is shown in Fig. S5a. All the diffraction peaks are consistent with the rhombohedral crystal structure, indicating that the obtained $NaCo_{0.5}Fe_{0.5}O_2$ sample belongs to an O3-type orthorhombic crystal structure. As shown in Fig. S5b, they were micrometer-sized particles in the range of 2–4 μm. Fig. 8a shows the charge and discharge curves of the $NaCo_{0.5}Fe_{0.5}O_2$ electrode in the potential range of 1.9–4.0 V at a constant current density of 20 mA $g^{-1}$. In the $NaCo_{0.5}Fe_{0.5}O_2$ electrode, the electrochemical reaction occurred through the $Co^{3+}/Co^{4+}$ and $Fe^{3+}/Fe^{4+}$ redox reactions at different potentials accompanied by a change in the crystal phase (O3 ↔ O3 + P3 ↔ P3 ↔ P′3 + O′3 ↔ O3′) [44]. The $NaCo_{0.5}Fe_{0.5}O_2$ electrode exhibited an initial discharge capacity of 136.1 mAh $g^{-1}$ with a coulombic efficiency of 92.4%. As shown in Fig. 8b, the $NaCo_{0.5}Fe_{0.5}O_2$ electrode showed good cycling behavior with a high columbic efficiency of 99.4% after initial cycles.

The superior electrochemical performance of the prepared $Fe_2GeO_4$@C anode and $NaCo_{0.5}Fe_{0.5}O_2$ cathode materials stimulated us to examine the realistic capability of a sodium-ion full cell that used them. Fig. S6 shows a schematic illustration of the sodium-ion cell with an $Fe_2GeO_4$@C anode and a $NaCo_{0.5}Fe_{0.5}O_2$ cathode. When assembling the full cell, the mass ratio of $Fe_2GeO_4$@C and $NaCo_{0.5}Fe_{0.5}O_2$ was optimized to 1.0:4.5 to obtain the best cycling performance. The assembled cell was first pre-conditioned at a low current density of 50 mA $g^{-1}$ based on the mass of the $Fe_2GeO_4$@C anode in the voltage range of 1.0–3.8 V for two cycles. After the pre-conditioning cycle, the cell was cycled at a constant current density of 200 mA $g^{-1}$. Fig. 9a shows the galvanostatic charge and discharge curves of the sodium-ion cell after the first pre-conditioning cycle. An initial discharge capacity of 311.3 mAh $g^{-1}$ was obtained based on the mass of the active $Fe_2GeO_4$@C material in the anode. Good cycling stability was achieved, with columbic efficiencies higher than 99.3%, as presented in Fig. 9b.

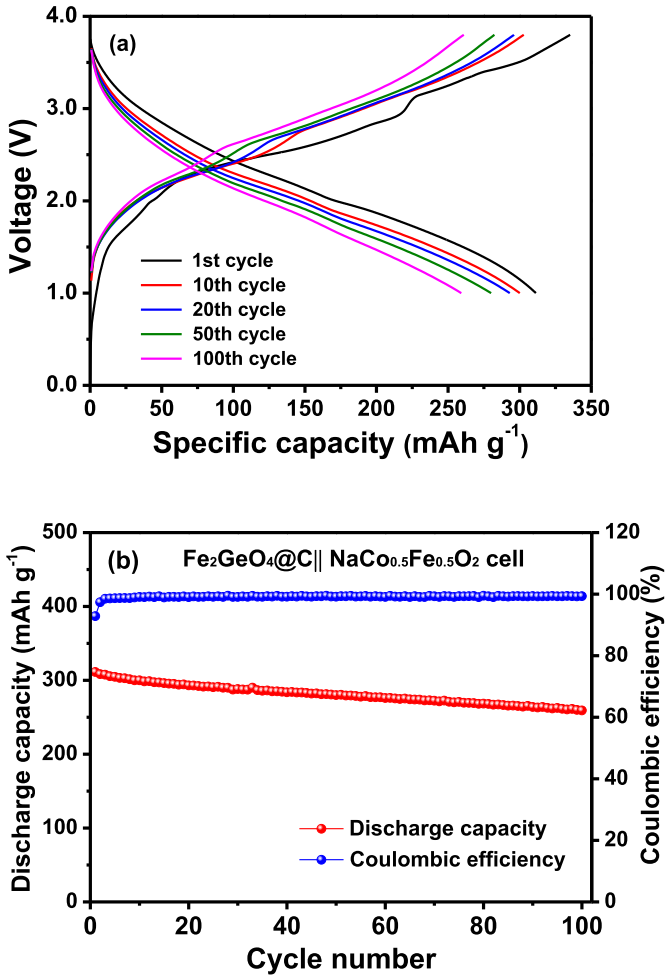


**Fig. 9.** (a) Charge and discharge curves of the sodium-ion cell with an $Fe_2GeO_4$@C anode and a $NaCo_{0.5}Fe_{0.5}O_2$ cathode. (b) Discharge capacity and coulombic efficiency of the sodium-ion cell as a function of the cycle number (cut-off voltage: 1.0–3.8 V).

Such a good cycling performance of the sodium-ion full cell demonstrates that the prepared $Fe_2GeO_4$@C material can be applied as a promising anode material for a sodium-ion battery.

## 4. Conclusions

In summary, we synthesized $Fe_2GeO_4$ and investigated its electrochemical performance as an anode material for sodium-ion batteries. The $Fe_2GeO_4$ electrode exhibited a relatively high discharge capacity with fast capacity fading. Its cycling stability could be improved by coating amorphous carbon onto the surface of the $Fe_2GeO_4$ particles. The carbon-coated $Fe_2GeO_4$ electrode delivered an initial capacity of 423.0 mAh $g^{-1}$ with a capacity retention of 89.0% after 100 cycles. The carbon coating helped to enhance the electron transport and relieve the volume strain during the sodiation and de-sodiation cycles. The sodium-ion full cell assembled with an $Fe_2GeO_4$@C anode and a $NaCo_{0.5}Fe_{0.5}O_2$ cathode exhibited good cycling performance in terms of the discharge capacity and cycling stability. Our results demonstrate that $Fe_2GeO_4$@C can be used as a promising anode material for sodium-ion batteries.

## Acknowledgements

This work was supported by the Basic Science Research Program of the National Research Foundation of Korea, funded by the Ministry of Science, ICT, and Future Planning (2016R1A4A1012224 and 2017R1A2A2A05020947).

## Appendix A. Supplementary data

Supplementary data to this article can be found online at https://doi.org/10.1016/j.matchemphys.2018.12.007.

## References

[1] M.M. Thackerey, C. Wolverton, E.D. Isaacs, Electrical energy storage for transportation-approaching the limits of and going beyond, lithium-ion batteries, Energy Environ. Sci. 5 (2012) 7854–7863.
[2] N. Nitta, F. Wu, J.T. Lee, G. Yushin, Li-ion battery materials: present and future, Mater. Today 18 (2015) 252–264.
[3] S. Goriparti, E. Miele, F.D. Angelis, E.D. Fabrizio, R.P. Zaccaria, C. Capiglia, Review on recent progress of nanostructured anode materials for Li-ion batteries, J. Power Sources 257 (2014) 421–443.
[4] D. Larcher, J.-M. Tarascon, Towards greener and more sustainable batteries for electrical energy storage, Nat. Chem. 7 (2015) 19–29.
[5] L. Li, Y. Zheng, S. Zhang, J. Yang, Z. Shao, Z. Guo, Research progress on sodium ion batteries: potential high-performance anodes, Energy Environ. Sci. 11 (2018) 2310–2340.
[6] Y. Cai, X. Cao, Z. Luo, G. Fang, F. Liu, J. Zhou, A. Pan, S. Liang, Caging $Na_3V_2(PO_4)_2F_3$ microcubes in cross-linked graphene enabling ultrafast sodium storage and long-term cycling, Adv. Sci. 5 (2018) 1800680.
[7] W. Luo, F. Shen, C. Bommier, H. Zhu, X. Ji, L. Hu, Na-ion battery anodes: materials and electrochemistry, Acc. Chem. Res. 49 (2016) 231–240.
[8] W. Wang, W. Li, S. Wang, Z. Miao, H.K. Liu, S. Chou, Structural design of anode materials for sodium-ion batteries, J. Mater. Chem. 6 (2018) 6183–6205.
[9] E. Irisarri, A. Ponrouch, M.R. Palacin, Review—Hard carbon negative electrode materials for sodium-ion batteries, J. Electrochem. Soc. 162 (2015) A2476–A2482.
[10] Y. Jiang, M. Hu, D. Zhang, T. Yuan, W. Sun, B. Xu, M. Yan, Transition metal oxides for high performance sodium ion battery anodes, Nano Energy 5 (2014) 60–66.
[11] N. Zhang, X. Han, Y. Liu, X. Hu, Q. Zhao, J. Chen, 3D porous γ-$Fe_2O_3$@C nanocomposite as high-performance anode material of Na-ion batteries, Adv. Energy. Mater. 5 (2015) 1401123–1401130.
[12] I. Sultana, M.M. Rahman, S. Mateti, V.G. Ahmadabadi, A.M. Glushenkov, Y. Chen, K-ion and Na-ion storage performances of $Co_3O_4$-$Fe_2O_3$ nanoparticle-decorated super P carbon black prepared by a ball milling process, Nanoscale 9 (2017) 3646–3654.
[13] M. Li, C. Ma, Q.-C. Zhu, S.-M. Xu, X. Wei, Y.-M. Wu, W.-P. Tang, K.-X. Wang, J.-S. Chen, Well-ordered mesoporous $Fe_2O_3$/C composites as high-performance anode materials for sodium-ion batteries, Dalton Trans. 46 (2017) 5025–5032.
[14] Y.V. Kaneti, J. Zhang, Y.-B. He, Z. Wang, S. Tanaka, M.S.A. Hossain, Z.-Z. Pan, B. Xiang, Q.-H. Yang, Y. Yamauchi, Fabrication of an MOF-derived heteroatom-doped Co/CoO/carbon hybrid with superior sodium storage performance for sodium-ion batteries, J. Mater. Chem. 5 (2017) 15356–15366.
[15] G. Fang, J. Zhou, Y. Cai, S. Liu, X. Tan, A. Pan, S. Liang, Metal-organic framework-templated two-dimensional hybrid bimetallic metal oxides with enhanced lithium/sodium storage capability, J. Mater. Chem. 5 (2017) 13983–13993.
[16] G. Fang, Z. Wu, J. Zhou, C. Zhu, X. Cao, T. Lin, Y. Chen, C. Wang, A. Pan, S. Liang, Observation of pseudocapacitive effect and fast ion diffusion in bimetallic sulfides as an advanced sodium-ion battery anode, Adv. Energy Mater. 8 (2018) 1703155.
[17] G.K. Veerasubramani, Y. Subramanian, M.-S. Park, G. Nagaraju, B. Senthilkumar, Y.-S. Lee, D.-W. Kim, Enhanced storage ability by using a porous pyrrhotite@N-doped carbon yolk-shell structure as an advanced anode material for sodium-ion batteries, J. Mater. Chem. 6 (2018) 20056–20068.
[18] M. Valvo, F. Lindgren, U. Lafont, F. Bjorefors, K. Edstrom, Towards more sustainable negative electrodes in Na-ion batteries via nanostructured iron oxide, J. Power Sources 245 (2014) 967–978.
[19] S. Yuvaraj, R. Kalai Selvan, Y.S. Lee, An overview of $AB_2O_4$- and $A_2BO_4$-structured negative electrodes for advanced Li-ion batteries, RSC Adv. 6 (2016) 21448–21474.
[20] W. Wang, Y. Sun, B. Liu, S. Wang, M. Cao, Porous carbon nanofiber webs derived from bacterial cellulose as an anode for high performance lithium ion batteries, Carbon 91 (2015) 56–65.
[21] X. Lai, J.E. Halpert, D. Wang, Recent advances in micro-/nano-structured hollow spheres for energy applications: from simple to complex systems, Energy Environ. Sci. 5 (2012) 5604–5618.
[22] H.-P. Feng, L. Tang, G.-M. Zeng, J. Tang, Y.-C. Deng, M. Yan, Y.-N. Liu, Y.-Y. Zhou, X.Y. Ren, S. Chen, Carbon-based core-shell nanostructured materials for electrochemical energy storage, J. Mater. Chem. 6 (2018) 7310–7337.
[23] P. He, Y. Fang, X.-Y. Yu, X.-W. Lou, Hierarchical nanotubes constructed by carbon-coated ultrathin SnS nanosheets for fast capacitive sodium storage, Angew. Chem. 56 (2017) 12202–12205.
[24] J.-W. Wen, D.-W. Zhang, Y. Zang, X. Sun, B. Cheng, C.-X. Ding, Y. Yu, C.-H. Chen, Li and Na storage behavior of bowl-like hollow $Co_3O_4$ microspheres as an anode material for lithium-ion and sodium-ion batteries, Electrochim. Acta 132 (2014) 193–199.
[25] M.M. Rahman, A.M. Glushenkov, T. Ramireddy, Y. Chen, Electrochemical investigation of sodium reactivity with nanostructured $Co_3O_4$ for sodium-ion batteries, Chem. Commun. 50 (2014) 5057–5060.
[26] J. Qin, N. Zhao, C. Shi, E. Liu, F. He, L. Ma, Q. Li, J. Li, C. He, Sandwiched C@

$SnO_2$@C hollow nanostructures as an ultralong-life span high-rate anode material for lithium-ion and sodium-ion batteries, J. Mater. Chem. 5 (2017) 10946–10956.
[27] Y. Liu, N. Zhang, C. Yu, L. Jiao, J. Chen, $MnFe_2O_4$@C nanofibers as high-performance anode for sodium-ion batteries, Nano Lett. 16 (2016) 3321–3328.
[28] Y.R. Lim, C.S. Jung, H.S. Im, K. Park, J. Park, W. Il Cho, E.H. Cha, $Zn_2GeO_4$ and $Zn_2SnO_4$ nanowires for high-capacity lithium- and sodium-ion batteries, J. Mater. Chem. 4 (2016) 10691–10699.
[29] D.-J. Xue, S. Xin, Y. Yan, K.-C. Jiang, Y.-X. Yin, Y.-G. Guo, L.-J. Wan, Improving the electrode performance of Ge through Ge@C Core−Shell nanoparticles and graphene networks, J. Am. Chem. Soc. 134 (2012) 2512–2515.
[30] S. Yuvaraj, K. Karthikeyan, R.K. Selvan, Facile hydrothermal synthesis and characterization of $Co_2GeO_4$/r-GO@C ternary nanocomposite as negative electrode for Li-ion batteries, J. Colloid Interface Sci. 498 (2017) 76–84.
[31] L. Jin, X. Li, H. Ming, H. Wang, Z. Jia, Y. Fu, J. Adkins, Q. Zhou, J. Zhang, Hydrothermal synthesis of $Co_3O_4$ with different morphologies towards efficient Li-ion storage, RSC Adv. 4 (2014) 6083–6089.
[32] C. Lai, Y.Y. Dou, X. Li, X.P. Gao, Improvement of the high rate capability of hierarchical structured $Li_4Ti_5O_{12}$ induced by the pseudocapacitive effect, J. Power Sources 195 (2010) 3676–3679.
[33] S. Li, X. Li, Y. Li, B. Yan, X. Song, L. Fan, H. Shan, D. Li, Design of $V_2O_5.xH_2O$ cathode for highly enhancing sodium storage, J. Alloy. Comp. 722 (2017) 278–286.
[34] T. Kajita, T. Itoh, Electrochemical sodium storage in amorphous $GeO_x$ powder, Electrochim. Acta 195 (2016) 192–198.
[35] Z. Jian, C. Bommier, L. Luo, Z. Li, W. Wang, C. Wang, P. Alex Greaney, X. Ji, Insights on the mechanism of Na-ion storage in soft carbon anode, Chem. Mater. 29 (2017) 2314–2320.
[36] S. Jin, C. Wang, Synthesis and first investigation of excellent lithium storage performances of $Fe_2GeO_4$/reduced graphene oxide nanocomposite, Nano Energy 7 (2014) 63–71.
[37] S. Yuvaraj, W.J. Lee, C.W. Lee, R. Kalai Selvan, In situ and ex situ carbon coated $Zn_2SnO_4$ nanoparticles as promising negative electrodes for Li-ion batteries, RSC Adv. 5 (2015) 67210–67219.
[38] J.-H. Kim, A.G. Kannan, H.-S. Woo, D.-G. Jin, W. Kim, K. Ryu, D.-W. Kim, A bifunctional metal-free catalyst composed of dual-doped graphene and mesoporous carbon for rechargeable lithium-oxygen batteries, J. Mater. Chem. 3 (2015) 18456–18465.
[39] D.A. Stevens, J.R. Dahn, The mechanisms of lithium and sodium insertion in carbon materials, J. Electrochem. Soc. 148 (2001) A803–A811.
[40] W. Wang, B. Tang, B. Ju, Z. Gao, J. Xiu, S. Zhang, $Fe_3O_4$-functionalized graphene nanosheet embedded phase change material composites: efficient magnetic- and sunlight-driven energy conversion and storage, J. Mater. Chem. 5 (2017) 958–968.
[41] S. Bhuvaneswari, P.M. Pratheeksha, S. Anandan, D. Rangappa, R. Gopalan, T.N. Rao, Efficient reduced graphene oxide grafted porous $Fe_3O_4$ composite as a high- performance anode material for Li-ion batteries, Phys. Chem. Chem. Phys. 16 (2014) 5284–5294.
[42] W. Wei, A. Tian, F. Jia, K. Wang, P. Qu, M. Xu, Green synthesis of $GeO_2$/graphene composites as anode material for lithium-ion batteries with high capacity, RSC Adv. 6 (2016) 87440–87445.
[43] W. Chen, K. Song, L. Mi, X. Feng, J. Zhang, S. Cui, C. Liu, Synergistic effect induced ultrafine $SnO_2$/graphene nanocomposite as an advanced lithium/sodium-ion batteries anode, J. Mater. Chem. 5 (2017) 10027–10038.
[44] H.-R. Yao, P.-F. Wang, Y. Wang, X. Yu, Y.-X. Yin, Y.-G. Guo, Excellent comprehensive performance of Na-based layered oxide benefiting from the synergetic contributions of multi metal ions, Adv. Energy Mater. 7 (2017) 1700189.